

Avalanche process in an idealized lamp: II. Modelling of breakdown in Ar/Xe electric discharges

Ananth N Bhoj¹ and Mark J Kushner^{2,3}

¹ Department of Chemical and Biomolecular Engineering, University of Illinois, 1406 W Green St., Urbana, IL 61801, USA

² Department of Electrical and Computer Engineering, University of Illinois, 1406 W Green St., Urbana, IL 61801, USA

E-mail: mjk@uiuc.edu.

Received 30 May 2004

Published 1 September 2004

Online at stacks.iop.org/JPhysD/37/2510

doi:10.1088/0022-3727/37/18/007

Abstract

The breakdown phase of the startup of metal halide lamps is typically through a cold fill of a rare gas and the ambient vapour pressure of a dose of metals. The dynamics of the breakdown stage are of interest for improving the efficiency and lifetime of lamps. A computational investigation of the breakdown of Ar/Xe mixtures in an idealized lamp geometry was performed using global and two-dimensional (2-d) models to provide insight into the lamp ignition processes and to facilitate comparison with experiments. The experimental trends for breakdown for pressures of 10–90 Torr were qualitatively captured with the global model. Quantitative agreement required accounting for the temporal and spatial plasma dynamics included in the 2-d model. Small fractions of Xe in Ar were found to decrease the breakdown time as the ionization rates increased due to the lower ionization potential of xenon, while the electron energy distribution was not significantly affected. With higher Xe fractions the electron temperature in the ionization front decreased due to there being larger momentum transfer and inelastic losses to the Xe, and as a result the breakdown times increased. The compression of voltage ahead of the ionization front produced large electric fields at the cathode that enabled significant contributions to ionization by secondary electrons.

1. Introduction

Metal halide high intensity discharge (HID) lighting sources are being used in an increasing number of applications as they have favourable colour renderings and high luminous efficiencies. The cold fill of HID lamps consists of tens to a few hundreds of Torr of rare gases, typically Ar, with doses of metal halide additives and/or mercury having a few milliTorrs vapour pressure at room temperature. In the steady state, HID lamps operate as thermal arcs producing quasi-continuum radiation from a multi-atmosphere, metal vapour plasma [1–5].

The starting sequence for the lamp begins with breakdown of the cold gas, often using multi-kilovolt pulses. The breakdown process consists of at least two phases, a statistical time lag and a formative time lag [6]. The statistical time lag is the average time required to generate seed electrons in the arc tube. The formative time lag is the time required for the growth of the electron density to a conductive state by ionization processes. Statistical time lags can have a wide variation, depending on the nature of the stochastic processes that produce seed electrons. Formative time lags are more deterministic, depending on the geometry, applied voltage and gas mixture. Strategies to reduce the statistical lag time in commercial lamps by preionization include the use of external

³ Author to whom any correspondence should be addressed.

ultraviolet (UV) light [1–3] and auxiliary electrodes and the addition of small quantities of radioactive ^{85}Kr .

Using large starting voltages can reduce the lifetime of lamps by increasing the rate of sputtering of electrodes, which in turn results in darkening of the tube and lumen loss [4]. Restarting of warm lamps requires larger restriking voltages, up to 20–30 kV, due to their higher gas pressures. Methods of improving restarting of warm lamps include controlled dimming techniques [7, 8], and electronic ballasts [2].

Breakdown is followed by a cold cathode phase in the presence of condensed metal vapour on the electrodes. In the absence of the condensed vapour, breakdown is directly followed by a glow discharge phase, which is characterized by a large cathode fall. Pitchford *et al* [5] used a one-dimensional model to investigate the breakdown and glow phases in HID lamps. They found that the voltage required to sustain the glow discharge was determined by the source impedance, gas composition and plasma density produced by the breakdown event. Lay *et al* [9] using a two-dimensional model, found that the capacitances of the walls of the discharge tube and placement of ground planes can affect the breakdown characteristics.

In this paper, we report on a computational investigation of the breakdown phase in Ar/Xe mixtures in an idealized geometry to facilitate comparison with the experiments reported in part I [10]. Ar/Xe mixtures have many of the qualitative characteristics of the Ar/Hg mixtures used in commercial lamps. The fact that commercial lamps often contain Hg with a rare gas buffer enables processes such as Penning ionization, which are likely to lower breakdown times compared with rare gases. Zero-dimensional (global) and two-dimensional (hereafter 0-d and 2-d) models were used in this study. Predictions from the global model qualitatively matched experimental trends; however, quantitative agreement required the more complete 2-d treatment of the plasma dynamics leading to breakdown. The electron avalanche starts at the biased electrode (anode) and propagates towards the grounded electrode (cathode). The electron temperature and electric fields in the ionization front ultimately determine the speed of avalanche and the breakdown time. The breakdown times decreased with small Xe fractions (10–15%) in Ar as the ionization rates increased due to the lower ionization potential of Xe. With higher Xe fractions the electron temperature decreases in the ionization front due to there being larger momentum transfer and inelastic losses. At higher pressures and lower voltages, a longer voltage ramp is required to reach the critical electric field required to initiate an electron avalanche.

The lamp geometry and reaction mechanism used in this study are described in section 2. The global and 2-d models are described in section 3. Results from the global and 2-d models are discussed in section 4 and section 5, respectively. Concluding remarks are presented in section 6.

2. Lamp geometry and reaction mechanism

Results from the models were compared with the measurements of breakdown times discussed in part I. The experiments were performed in Ar/Xe mixtures using a model geometry

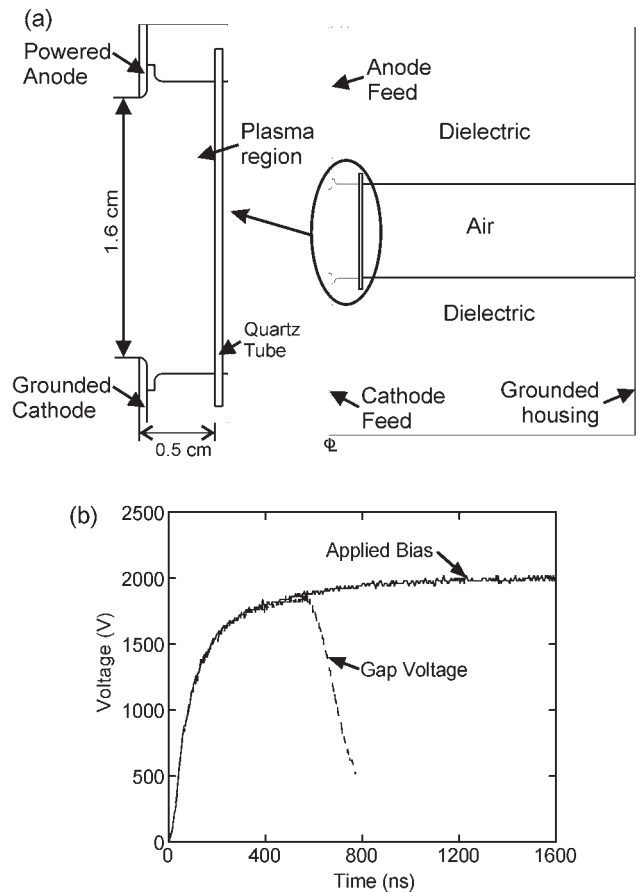


Figure 1. An experimental discharge tube closely resembling the dimensions of a commercial HID lamp was modelled to be 2-d, cylindrically symmetric. (a) Schematic of the experimental geometry, with the arc tube region enlarged. The inter-electrode spacing is 1.6 cm. (b) The experimental 2000 V waveform showing the decrease in gap voltage at breakdown.

closely resembling that of a commercial polycrystalline alumina [11] HID lamp. A schematic of the cylindrically symmetric lamp is shown in figure 1(a). The upper electrode is the biased anode, and the lower electrode is the grounded cathode. The quartz tube has an inner diameter of 1.0 cm and the inter-electrode separation is 1.6 cm. Details of the experiments are discussed in part I [10].

A typical experimental voltage waveform is shown in figure 1(b). The amplitude of the applied voltage, V_0 , is defined as the asymptotically approached value for the open circuit. The time to breakdown is denoted by the time that the voltage across the gap decreases to 95% of its most recent maximum value. The voltage drop across the gap results from the current flow through an 11.5 k Ω ballast resistor. A preionization electron density was provided by electrons surviving from the previous pulse and external illumination from a UV lamp. The pulse repetition frequency in the experiments was 1 Hz, chosen to minimize the statistical time lag while operating with as small a preionization density as possible. In our computational investigation, we modelled only a single pulse, while specifying a preionization electron and ion density produced by the external illumination.

The Ar/Xe reaction mechanism used in the global and 2-d models is listed in table 1. The Ar(4s) excited state is denoted

Table 1. Ar/Xe reaction mechanism.

	<i>Species</i>	
e	Xe	ArXe*
Ar*(4s)	Xe*(6s)	ArXe*
Ar**(4p)	Xe**(6p)	
Ar ⁺	Xe*** (6s')	
Ar ₂ [*]	Xe ₂ ⁺	
Ar ₂ ⁺	Xe ₂ [*]	
	Xe ₂ ⁺	
Reaction	Rate coefficient ^a	Ref.
e + Ar → Ar + e	^b	[12]
e + Ar → Ar* + e	^b	[13]
e + Ar → Ar** + e	^b	[13]
e + Ar → Ar ⁺ + e + e	^b	[14]
e + Ar* → Ar ⁺ + e + e	^b	[15]
e + Ar** → Ar ⁺ + e + e	^b	[16]
e + Ar ₂ [*] → Ar ₂ ⁺ + e + e	$9.0 \times 10^{-8} T_e^{0.7} e^{-3.66/T_e}$	[17]
e + Ar ₂ ⁺ → Ar ₂ [*] + e	^b	[18]
e + Ar* → Ar + e	^{b,c}	[13]
e + Ar** → Ar + e	^b	[13]
e + Ar** → Ar* + e	^b	[18]
e + Ar ₂ ⁺ → Ar** + Ar	$5.38 \times 10^{-8} T_e^{-0.66}$	[17]
e + Ar ₂ ⁺ → Ar + Ar + e	1.0×10^{-7}	[17]
e + Ar ₂ ⁺ → Ar*	$4.0 \times 10^{-13} T_e^{-0.5}$	[19]
e + e + Ar ⁺ → Ar** + e	$5.0 \times 10^{-27} T_e^{-4.5} \text{ cm}^6 \text{ s}^{-1}$	[19]
e + Xe → Xe + e	^b	[12]
e + Xe → Xe* + e	^b	[20]
e + Xe → Xe** + e	^b	[21]
e + Xe* → Xe** + e	^b	[22]
e + Xe → Xe ⁺ + e + e	^b	[14]
e + Xe* → Xe ⁺ + e + e	^b	[22]
e + Xe** → Xe ⁺ + e + e	^b	[22]
e + Xe ₂ [*] → Xe ₂ ⁺ + e + e	$9.75 \times 10^{-8} T_e^{0.71} e^{-3.40/T_e}$	[23]
e + Xe ₂ ⁺ → Xe + e	^b	[20]
e + Xe** → Xe* + e	^b	[22]
e + Xe** → Xe + e	^b	[22]
e + Xe ₂ ⁺ → Xe* + Xe	$0.37 \times 10^{-7} T_e^{-0.5}$	[19] ^d
e + Xe ₂ ⁺ → Xe** + Xe	$0.37 \times 10^{-7} T_e^{-0.5}$	[19] ^d
e + Xe → Xe*** + e	^b	[24]
e + Xe*** → Xe ⁺ + e + e	$1.56 \times 10^{-7} T_e^{0.71} e^{-2.63/T_e}$	[23]
e + Xe*** → Xe** + e	$5.50 \times 10^{-7} T_e^{0.79} e^{-2.0/T_e}$	[23] ^d
e + Xe*** → Xe + e	^b	[24]
e + Xe ₂ ⁺ → Xe*** + Xe	$3.33 \times 10^{-7} T_e^{-0.5}$	[19] ^d
e + ArXe* → Xe** + Ar	$1.0 \times 10^{-7} T_e^{0.5}$	[17]
e + ArXe* → Xe + Ar + e	1.0×10^{-10}	[23]
Ar ⁺ + Ar → Ar + Ar ⁺	4.60×10^{-10}	[25] ^e
Ar* + Ar + Ar → Ar ₂ [*] + Ar	$1.14 \times 10^{-32} \text{ cm}^6 \text{ s}^{-1}$	[17]
Ar** + Ar + Ar → Ar ₂ [*] + Ar	$1.14 \times 10^{-32} \text{ cm}^6 \text{ s}^{-1}$	[17]
Ar ⁺ + Ar + Ar → Ar ₂ ⁺ + Ar	$2.50 \times 10^{-31} \text{ cm}^6 \text{ s}^{-1}$	[17]
Ar ₂ [*] → Ar + Ar	$6.0 \times 10^7 \text{ s}^{-1}$	[17]
Ar ₂ ⁺ → Ar	$2.0 \times 10^6 \text{ s}^{-1}$	[17] ^d
Ar* → Ar	$1.0 \times 10 \text{ s}^{-1}$	[26] ^f
Ar* + Ar* → Ar ⁺ + Ar + e	1.0×10^{-9}	[17]
Ar* + Ar** → Ar ⁺ + Ar + e	1.0×10^{-9}	[17] ^g
Ar** + Ar** → Ar ⁺ + Ar + e	1.0×10^{-9}	[17] ^g
Ar ₂ [*] + Ar ₂ [*] → Ar ₂ ⁺ + Ar + Ar + e	5.0×10^{-10}	[17] ^d
Xe ⁺ + Xe → Xe + Xe ⁺	3.60×10^{-10}	[17] ^d
Xe* + Xe + Xe → Xe ₂ ⁺ + Xe	$5.0 \times 10^{-32} \text{ cm}^6 \text{ s}^{-1}$	[23]
Xe** + Xe + Xe → Xe ₂ ⁺ + Xe	$5.0 \times 10^{-32} \text{ cm}^6 \text{ s}^{-1}$	[23] ^g
Xe ₂ [*] → Xe + Xe	$7.22 \times 10^7 \text{ s}^{-1}$	[23]
Xe ₂ ⁺ → Xe	$2.34 \times 10^0 \text{ s}^{-1}$	[26] ^f
Xe** → Xe*	$0.50 \times 10^7 \text{ s}^{-1}$	[17] ^d
Xe* + Xe* → Xe ⁺ + Xe + e	5.0×10^{-10}	[23]
Xe** + Xe** → Xe ⁺ + Xe + e	5.0×10^{-10}	[23] ^g
Xe ⁺ + Xe + Xe → Xe ₂ ⁺ + Xe	$2.50 \times 10^{-31} \text{ cm}^6 \text{ s}^{-1}$	[23]
Xe*** + Xe + Xe → Xe ₂ ⁺ + Xe	$5.0 \times 10^{-32} \text{ cm}^6 \text{ s}^{-1}$	[17] ^d
Xe*** → Xe	$5.49 \times 10^6 \text{ s}^{-1}$	[17] ^d
Xe** → Xe***	$0.50 \times 10^7 \text{ s}^{-1}$	[17] ^d

Table 1. (Continued.)

Xe*** + Xe*** → Xe ⁺ + Xe + e	5.0×10^{-10}	^d
Ar* + Xe → Ar + Xe*	2.10×10^{-10}	[17]
Ar** + Xe → Ar + Xe ⁺ + e	2.0×10^{-10}	[23]
Ar ⁺ + Xe → Ar + Xe ⁺	4.30×10^{-13}	[27]
Xe* + Xe + Ar → Xe ₂ [*] + Ar	$2.30 \times 10^{-32} \text{ cm}^6 \text{ s}^{-1}$	[23] ^d
Xe** + Xe + Ar → Xe ₂ [*] + Ar	$2.30 \times 10^{-32} \text{ cm}^6 \text{ s}^{-1}$	[23] ^d
Xe ⁺ + Xe + Ar → Xe ₂ ⁺ + Ar	$2.0 \times 10^{-31} \text{ cm}^6 \text{ s}^{-1}$	[23] ^d
Ar* + Ar + Xe → Ar ₂ [*] + Xe	$1.10 \times 10^{-32} \text{ cm}^6 \text{ s}^{-1}$	[17] ^d
Ar** + Ar + Xe → Ar ₂ [*] + Xe	$1.10 \times 10^{-32} \text{ cm}^6 \text{ s}^{-1}$	[17] ^d
Ar ⁺ + Ar + Xe → Ar ₂ ⁺ + Xe	$2.0 \times 10^{-31} \text{ cm}^6 \text{ s}^{-1}$	[17] ^d
Ar* + Xe + Xe → Xe ₂ [*] + Ar	$1.0 \times 10^{-33} \text{ cm}^6 \text{ s}^{-1}$	[17] ^d
Ar** + Xe + Xe → Xe ₂ [*] + Ar	$1.0 \times 10^{-33} \text{ cm}^6 \text{ s}^{-1}$	[17] ^d
Ar ₂ ⁺ + Xe → Xe ⁺ + Ar + Ar	1.25×10^{-9}	[27]
Ar* + Xe → ArXe*	5.0×10^{-11}	[23]
Ar** + Xe → ArXe*	5.0×10^{-11}	[23] ^g
Ar ₂ ⁺ + Xe → ArXe* + Ar	5.0×10^{-11}	[23]
Ar ⁺ + Xe + Ar → ArXe ⁺ + Ar	$1.0 \times 10^{-31} \text{ cm}^6 \text{ s}^{-1}$	[23]
Ar* + Xe + Xe → ArXe ⁺ + Xe	$1.0 \times 10^{-31} \text{ cm}^6 \text{ s}^{-1}$	[23] ^d
ArXe ⁺ + Xe → Xe ⁺ + Ar + Xe	5.0×10^{-10}	[23]
ArXe ⁺ + Xe → Xe ₂ ⁺ + Ar	1.0×10^{-11}	[23]
ArXe* + Xe → Xe ₂ ⁺ + Ar	1.0×10^{-10}	[23]
ArXe* → Ar + Xe	$5.0 \times 10^7 \text{ s}^{-1}$	[23]
Xe ⁺ + Ar + Ar → ArXe ⁺ + Ar	$1.0 \times 10^{-31} \text{ cm}^6 \text{ s}^{-1}$	[23]
Xe* + Ar + Ar → ArXe* + Ar	$1.0 \times 10^{-33} \text{ cm}^6 \text{ s}^{-1}$	[23]
Xe*** + Xe + Ar → Xe ₂ [*] + Ar	$2.30 \times 10^{-32} \text{ cm}^6 \text{ s}^{-1}$	[17] ^d
$h\nu$ + Xe → Xe ⁺ + e	$1.0 \times 10^{-14} \text{ cm}^2$	^h
M ⁺ → wall → M	ⁱ	
M* → wall → M	ⁱ	

^a Rate coefficients have unit of $\text{cm}^3 \text{ s}^{-1}$ unless noted otherwise.

Electron temperatures are in eV.

^b The rate coefficient was obtained by solving Boltzmann's equation for the EED. Cross sections for the process are from the indicated reference.

^c Cross section and rate coefficient obtained by detailed balance.

^d Estimated.

^e Determined from mobility of ion in Ar.

^f Trapped rate.

^g Approximated by analogy.

^h See text.

ⁱ In wall reactions, all ions recombine to their neutral counterparts and all excited states quench to the ground state.

as Ar*. Higher excited states (Ar(4p) and others) are lumped together and denoted as Ar**. Three lumped excited states of Xe are included: Xe*(6s states), Xe**(6p states) and Xe*** (6s' states). At the pressures of interest, three-body collisions are significant, and so the neutral dimer species Ar₂^{*}, Xe₂^{*} and ArXe* are also included. Charged species include electrons, Ar⁺ and Xe⁺ and the dimer ions Ar₂⁺, Xe₂⁺ and ArXe⁺.

Although the ionization potential of Xe (12.3 eV) is smaller than that of Ar (15.8 eV), Ar/Xe is not a classic Penning mixture. The lowest excitation energy of the metastable states Ar(4s), 11.6 eV, is insufficient to Penning ionize Xe. The Ar(4p) manifold (minimum energy 13.1 eV) can, however, Penning ionize Xe. The rate coefficient for charge exchange from Ar⁺ to Xe is unusually small [27], $4.3 \times 10^{-13} \text{ cm}^3 \text{ s}^{-1}$, and so significant charge exchange on the timescale of breakdown (hundreds of nanoseconds to 1 μs) occurs only for the upper range of pressure (90 Torr) and Xe mole fractions investigated. A more likely route to charge exchange from Ar⁺ to Xe with small mole fractions of Xe is dimerization to form Ar₂⁺ followed by charge exchange to Xe (rate coefficient $1.25 \times 10^{-9} \text{ cm}^3 \text{ s}^{-1}$, or a lifetime of less than tens of nanoseconds for the conditions of interest) [27]. Even

this route is important only at the upper ranges of pressure. (A rate coefficient of $2.5 \times 10^{-31} \text{ cm}^6 \text{ s}^{-1}$ produces a $1 \mu\text{s}$ lifetime for dimerization of Ar^+ at 60 Torr.)

3. Description of the models

The 0-d model GLOBAL_KIN [28] represents the plasma chemistry and kinetics of a discharge on a volume averaged basis. As such, the model is the analogue of the well-stirred-reactor model often used to model batch reactors. The weakness of a global model is that it can only approximately address spatially dependent phenomena using, for example, diffusion lengths or electric field enhancement factors. The strength of the global model is that it can be rapidly executed and so larger parameterizations can be performed. GLOBAL_KIN has three main modules: a plasma chemistry module, a circuit module and a module that solves Boltzmann's equation for the electron energy distribution (EED). Based on the reaction mechanism, the plasma chemistry module constructs differential equations for the evolution of species densities and the electron temperature. The circuit module addresses the currents and voltages in the external circuit and ultimately the E/N (electric field strength/gas number density) in the plasma.

The source terms for gas phase reactions are obtained from species concentrations and reaction rate coefficients using

$$\frac{dn_i}{dt} = \sum_j \left\{ (a_{ij}^2 - a_{ij}^1) k_j \prod_l n_l^{a_{lj}^1} \right\} - \frac{D_i n_i s_i}{\Lambda^2} + \sum_j \frac{D_j n_j \gamma_{ji}}{\Lambda^2}, \quad (1)$$

where a_{ij}^1 and a_{ij}^2 are the left-hand side and right-hand side stoichiometric coefficients of species i in reaction j , n_i is the density of species i and k_j is the rate constant of reaction j . The diffusion coefficient is D_i , and the diffusion length is Λ . The loss probability for species i diffusing to a surface is s_i , and the branching for its production at the surface by species j is γ_{ij} . Charged particles diffuse with rates consistent with ambipolar diffusion when charge densities are sufficiently large.

Rate coefficients for neutral and ion–molecule heavy particle reactions are calculated using Arrhenius expressions. The rate constants for electron impact reactions are obtained as a function of the electron temperature by solving the two-term spherical harmonic expansion for Boltzmann's equation for the EED [29]. The EED is computed for a range of values of E/N , from which rate coefficients and the electron temperature are obtained. (For non-Maxwellian EEDs, $T_e = \frac{2}{3}(\epsilon)$.) The resulting table is then interpolated for transport coefficients based on the instantaneous electron temperature. The external circuit consists of a ballast resistor of $11.5 \text{ k}\Omega$ and a power supply that provides the experimental voltage waveform.

The electron temperature is determined by the energy gained from Joule heating and energy lost in elastic and inelastic collisions,

$$\frac{d}{dt} \left(\frac{3}{2} n_e k_B T_e \right) = \vec{j} \cdot \vec{E} - \sum_i \frac{3}{2} n_e \nu_{mi} \left(\frac{2m_e}{M_i} \right) k_B (T_e - T_i) - \sum_i n_e k_i N_i \Delta \epsilon_i, \quad (2)$$

where n_e is the electron density, T_e is the electron temperature, and \vec{j} and \vec{E} are the current density and electric field in the discharge, respectively. ν_{mi} is the electron momentum transfer collision frequency with species i , m_e is the electron mass and M_i and T_i are the mass and temperature of species i . For the i th electron impact process, k_i is the reaction rate coefficient, N_i is the density of the heavy species collision partner and $\Delta \epsilon_i$ is the change in electron energy.

The average gas temperature is obtained by taking into account the heating from elastic and inelastic collisions with electrons (e.g., Frank–Condon heating), the enthalpy of heavy particle reactions and heat transfer to surfaces,

$$\begin{aligned} \frac{d}{dt} (N c_p T_g) &= \sum_i \frac{3}{2} n_e \nu_{mi} \left(\frac{2m_e}{M_i} \right) k_B (T_e - T_i) \\ &+ \sum_j n_e k_j N_j \Delta \epsilon_j - \sum_j \Delta H_j R_j \\ &= h_{\text{eff}} \frac{T_g - T_w}{\Lambda^2}, \end{aligned} \quad (3)$$

where N is the total gas density, c_p is the specific heat, and ΔH_j and R_j are the change in enthalpy and rate of the j th reaction. h_{eff} is the effective heat transfer coefficient for thermal conduction to the discharge tube walls having temperature T_w , and Λ is the thermal diffusion length. The resulting set of ordinary differential equations is integrated in time using VODE, a stiff equation solver [30].

The 2-d model LAMPSIM has been described in detail elsewhere [9, 31] and so only its principal features will be discussed here. LAMPSIM uses a 2-d unstructured mesh that is made using the commercial mesh generator Skymesh2 [32]. The electric potential is solved for over the entire mesh. Species densities and fluxes, the electron temperature and the gas temperature are computed only in the gas phase region within the discharge tube. Surface charge is computed only on dielectric materials. The fundamental equations that are solved are

$$-\nabla \cdot \epsilon \nabla \Phi = \sum_j N_j q_j + \rho_s, \quad (4)$$

$$\frac{\partial N_i}{\partial t} = -\nabla \cdot \vec{\phi}_i + S_i, \quad (5)$$

$$\frac{\partial \rho_s}{\partial t} = \sum_i -\nabla \cdot (q_i \vec{\phi}_i (1 + \gamma_i)) - \nabla \cdot (\sigma (-\nabla \Phi)), \quad (6)$$

where ϵ , Φ , ρ_s , N , ϕ , γ , σ , S and q are the permittivity, electric potential, surface charge density, species number density, species flux, electron secondary emission coefficient, conductivity of solid materials, source terms and elementary charge respectively. The subscript denotes the identity of the species. The Poisson equation (equation (4)) describing the electric potential, transport equations for conservation of the charged species (equation (5)) and surface charge balance (equation (6)) are simultaneously solved. We assume that all charged species neutralize on surfaces.

Fluxes for charged species are computed using the Scharfetter–Gummel formulation [33]. In this method, the flux between mesh points i and $(i + 1)$ separated by Δx is

$$\vec{\phi}_{i+1/2} = \alpha \bar{D} \left(\frac{n_{i+1} - n_i \exp(\alpha \Delta x)}{1 - \exp(\alpha \Delta x)} \right), \quad (7)$$

where

$$\alpha = \frac{(q/|q|)\bar{\mu}((\Phi_{i+1} - \Phi_i)/\Delta x)}{\bar{D}} \quad (8)$$

and $\bar{\mu}$ and \bar{D} are the average mobility and diffusion coefficient in the interval.

Equations (4)–(6) were solved using finite volume discretization and employing an implicit Newton's method to integrate in time. The resulting sparse matrix was inverted using the numerical package *dsluacs*, obtained from the SLAP Sparse Matrix Library [34, 35].

The densities of neutral species are obtained from

$$\frac{dN_i}{dt} = -\nabla \cdot \bar{\phi}_i + S_i + \left[(-\nabla \cdot \bar{\phi}_i)S_i + \sum_j (\nabla \cdot \bar{\phi}_j)\gamma_{ji}S_j \right]_s, \quad (9)$$

where for neutral species $\bar{\phi}_i = -D_i \nabla N_i$, D_i is the diffusion coefficient and S_i is the source due to all processes. The bracketed term accounts for surface reactions and is only included at surface nodes. The summation is over both charged and neutral species. Neutral densities are updated implicitly in a time splicing manner following the update of charged species densities and the electric potential using successive-over-relaxation techniques. Surface chemistry is addressed using a flux-in/flux-out boundary condition. Of the total flux of species i striking a surface, a fraction s_i is lost and a fraction γ_{ij} returns to the plasma as species j , as in the global model.

The initial densities for all excited states, charge densities and potentials are zero. The initial electron and ion densities are uniform with a specified density (see below), with the ions in proportion to their parent mole fractions.

Production of electrons ahead of the avalanche front can occur from photoionization. Photoionization comes from two sources, plasma generated photons and photons from the external UV lamp. The photoionization source by plasma-generated photons for species m , $S_m(\vec{r}_i)$, at location \vec{r}_i due to photons emitted from location \vec{r}'_j is

$$S_m(\vec{r}_i) = N_m(\vec{r}_i) \sum_k \sigma_{mk} A_k \int N_k(\vec{r}'_j) G_k(\vec{r}'_j, \vec{r}_i) d^3 \vec{r}'_j, \quad (10)$$

$$G_k(\vec{r}'_j, \vec{r}_i) = \frac{\exp(-\int_{\vec{r}'_j}^{\vec{r}_i} \sum_l \sigma_{lk} N_l(\vec{r}'_n) d\vec{r}'_n)}{4\pi |\vec{r}'_j - \vec{r}_i|^2}, \quad (11)$$

where N_k is the density of the k th radiating species having Einstein coefficient A_k , σ_{mk} is the photoionization cross section for species m by photon k , and σ_{lk} is the total absorption cross section for photon k by species l . $G_k(\vec{r}'_j, \vec{r}_i)$ is a Green's function for the survival of photons emitted at location \vec{r}'_j to \vec{r}_i and also accounts for view angles and obscurations. In this study, resonant radiation from Ar(4s) was the source of the ionizing photon flux, and a photoionization cross section of 100 \AA^2 was used for Xe.

Photoemission produced by fluxes of photons incident on the electrodes from both plasma generated and external sources was included. The fluxes of plasma-generated photons incident onto the electrodes, $\phi_P(\vec{r}_i)$, was obtained

by integrating photon sources throughout the volume and convolving with $G_k(\vec{r}'_j, \vec{r}_i)$:

$$\phi_P(\vec{r}_i) = \sum_k A_k \int N_k(\vec{r}'_j) G_k(\vec{r}'_j, \vec{r}_i) d^3 \vec{r}'_j. \quad (12)$$

The flux of externally generated photons was specified based on the characteristics of the pen-lamp used in the experiments (2 W lamp producing 254 nm photons with a 10% efficiency placed 2 cm from the electrodes). The photoemission of electrons from the electrodes with a probability of 0.1 per incident photon was then added. For emission from the anode, these sources were added to the continuity equation for electrons as a flux emanating from the surface having a Lambertian angular distribution. Photoelectrons emitted from the cathode were addressed using the Electron Monte Carlo Module (EMCM).

The electron energy equation is solved for the average energy, ε , of the bulk electrons,

$$\frac{d}{dt}(n_e \varepsilon) = \vec{j} \cdot \vec{E} - n_e \sum_i N_i \kappa_i - \nabla \cdot \left(\frac{5}{2} \varepsilon \vec{\phi}_e - \lambda \nabla T_e \right), \quad (13)$$

$$\vec{j} = q \vec{\phi}_e,$$

where T_e is the electron temperature, n_e is the electron density, κ_i is the rate coefficient for power loss for collisions of electrons with species i having density N_i , λ is the electron thermal conductivity and $\vec{\phi}_e$ is the electron flux obtained from equation (7). The electron temperature is obtained by implicitly integrating equation (12) in time using a successive-over-relaxation technique following updates of equations (4)–(6). The initial electron temperature was 0.03 eV as was the electron temperature on boundaries. The electron transport coefficients and rate coefficients as a function of T_e are obtained by solving Boltzmann's equation in the same manner as in GLOBAL-KIN.

Trajectories of secondary electrons emitted from surfaces were followed with the EMCM, which is described in detail in [31]. The EMCM is performed on a separate Cartesian sub-mesh that is appropriately defined near electron-emitting surfaces. Particles are released from electron emitting nodes on the unstructured mesh and their trajectories are advanced using electric fields that are interpolated from the unstructured mesh onto the structured mesh. Statistics on the trajectory of the electrons are collected on the structured mesh to compute EEDs as a function of position. Those electrons that fall in energy below a specified threshold are removed from the simulation and added to the bulk electrons. The results of the EMCM are electron impact source functions and sources of secondary electrons calculated from the EEDs of the beam electrons and their progeny. These electron impact sources are then included in the continuity equations for charged and neutral species in the fluid portion of the model. The EMCM is called at specified time intervals, and the sources due to electron impact by beam electrons are held constant in the fluid model between calls to the EMCM.

The EMCM was run every 2 ns during the simulation. Two hundred and fifty pseudoparticles were released from each mesh point on the surface of the cathode (of which there are 25) for each run of the EMCM. Ionization by these pseudoparticles increases the initial allocation by factors of as much as 4–5.

The statistical weighting of the pseudoparticles used to obtain the EEDs is in proportion to the flux of photons and ions incident onto the cathode. A secondary electron emission coefficient of 0.15 was used for all ions.

The circuit model provides the electric potential boundary conditions applied to the metal surfaces. A ballast resistor of $11.5\text{ k}\Omega$ is used in series with the discharge.

4. Breakdown trends from the global model

Trends in the breakdown times in Ar/Xe mixtures were first investigated using GLOBAL_KIN while varying the gas pressure, composition and applied bias. The initial conditions were that all excited state densities and the voltage across the discharge tube are zero. The electron and ion densities were 50 cm^{-3} (with the ion densities distributed in proportion to their parent gases), though the systematic trends were not sensitive to this value, as discussed below. The mean breakdown time (τ) obtained with the global model as a function of pressure for Ar/Xe = 95/5 and $V_0 = 2000\text{ V}$ is shown in figure 2(a). Comparisons are made with the experiments discussed in part I. The electron temperatures for 10 and 90 Torr are shown in figure 3. The results from the global model systematically reproduce the experimental trends of increasing τ with increasing pressure, though the calculated results under-predict the experiments. The increase in τ results, to first order, simply from the longer time required for the same voltage waveform to reach a critical value of E/N to initiate an avalanche as the pressure increases.

The electron temperature at 10 Torr peaks at 5.2 eV, whereas that at 90 Torr peaks at 3.5 eV. In principle, particularly in the context of the global model, breakdown should depend only on achieving a critical E/N [denoted $(E/N)_0$] that provides a sufficiently large electron temperature to initiate an avalanche. The larger T_e at 10 Torr compared with 90 Torr indicates an overshoot in the applied E/N above $(E/N)_0$. As discussed in part I, this overshoot could result from non-negligible diffusion losses for avalanching electrons at 10 Torr. Overshoot could also result from the fact that at 10 Torr, the time required to avalanche the preionization electron density to the breakdown value is commensurate to the voltage ramp-up time. Breakdown is also indicated by the decrease in T_e in figure 3 to a lower self-sustaining value as the voltage drops across the gap. The larger value of τ at 90 Torr is reflected by the longer plateau in T_e near its peak prior to falling to its self-sustaining value after breakdown. Note that the prebreakdown, plateau value of T_e is lower at 90 Torr, thereby requiring a longer induction time to avalanche the electron density to the value that a critical current flows that signifies breakdown.

Breakdown times as a function of V_0 are shown in figure 2(b) for Ar/Xe = 90/10 at 10 Torr. The larger E/N at higher voltages increases ionization rates, leading to shorter breakdown times. Experimentally, the effect of voltage on breakdown times is more pronounced at lower voltages. The model reproduces the experimental trends but again under-predicts breakdown times at lower voltages and has a weaker dependence on the applied voltage. Electron temperatures for Ar/Xe = 95/5 at 90 Torr with $V_0 = 1500$ and 2000 V are shown in figure 3. During the prebreakdown, plateau induction time, there is a small decrease in T_e from 3.72 eV

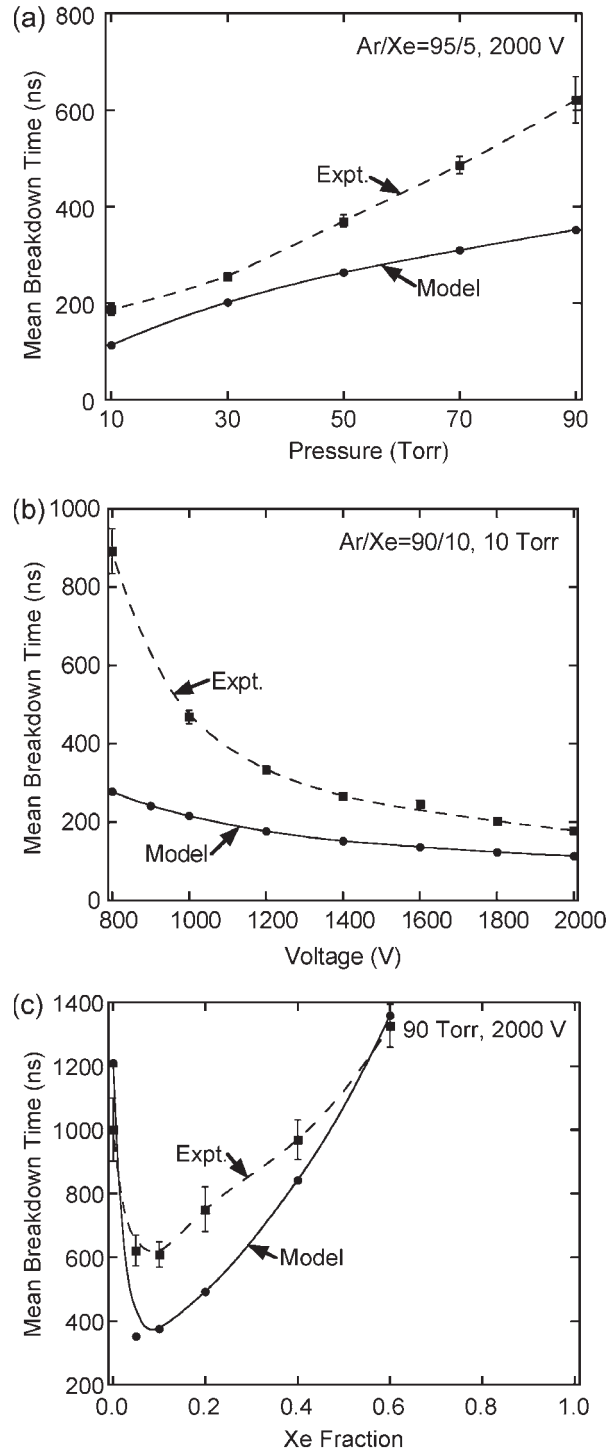


Figure 2. Time to breakdown, τ , obtained from the global model. (a) Ar/Xe = 95/5, $V_0 = 2000\text{ V}$ as a function of pressure, (b) Ar/Xe = 90/10, 10 Torr as a function of applied voltage; and (c) 90 Torr, $V_0 = 2000\text{ V}$ as a function of composition of the Ar/Xe mixture. Comparisons made with experiments reproduce trends but under-predict τ .

at $V_0 = 2000\text{ V}$ to 3.6 eV at $V_0 = 1500\text{ V}$, thereby requiring a somewhat longer time to avalanche from the preionization density to a critical current density that signifies breakdown.

Breakdown times vary non-monotonically with gas composition as shown in figure 2(c). Small fractions of

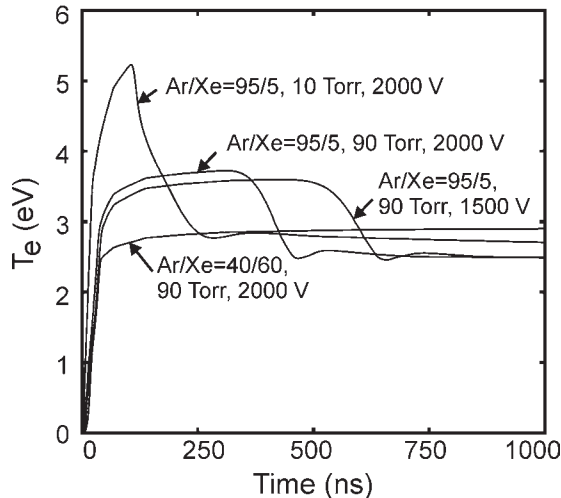


Figure 3. Electron temperature as a function of time obtained from the global model for different gas mixtures and charging voltage, V_0 . Due to the overshoot of $(E/N)_0$, T_e can exceed the self-sustaining value.

Xe generally decrease breakdown times relative to pure Ar, whereas large additions of Xe increase the breakdown time. For example, at 90 Torr and $V_0 = 2000$ V, the breakdown time decreases from 1210 ns in Ar to 350 ns with Ar/Xe = 95/5. There is little change in the breakdown time for Xe fractions of 5–20%. The breakdown time increases for Xe fractions >15–20%. Again, the global model captures the qualitative trends but fails to quantitatively predict breakdown times as τ is underpredicted.

The addition of Xe generally lowers the electron temperature as shown in figure 3. As discussed in part I, with small Xe fractions the decrease in electron temperature is compensated by the lower ionization potential of Xe (12.3 eV) compared with Ar (15.8 eV). The small addition of Xe then produces larger net rates of ionization in spite of the smaller T_e . With larger mole fractions of Xe, the decrease in electron temperature is sufficiently large for the ionization rates to decrease in spite of there being a large mole fraction of Xe having a lower ionization threshold. Similar trends are obtained at other pressures and voltages. In general, the consequences of varying the composition are more dramatic at higher pressures, where with small fractions of Xe (5–20%) τ can decrease by up to a factor of 2.

Breakdown times predicted by the global model generally capture the experimental trends; however, the predictions are not quantitatively correct and in general under-predict τ . In investigating this discrepancy, the preionization density and circuit inductances and capacitances were varied. In particular, the initial electron and ion densities were varied from 1 to 10^7 cm^{-3} . In general, changing the initial electron density produced a small shift (a few nanoseconds to 20 ns) in the breakdown time, providing shorter breakdown times for larger initial electron densities. This was generally the trend as long as the initial electron density was small compared with the density required to conduct sufficient current to alter the discharge voltage ($>10^{10}$ cm^{-3}). The exception was at high pressures (70–90 Torr), high Xe concentrations (>30–40%) and low voltages (<1200 V), where the breakdown time could

be decreased by hundreds of nanoseconds by varying the initial densities by $1\text{--}10^7$ cm^{-3} . This is in a regime where, experimentally, breakdown could not be obtained or was at best sporadic.

The reaction mechanism was also parameterized by including or excluding sets of reactions. For example, when excluding electron impact ionization from excited states or Penning reactions, the conduction phase following breakdown was significantly affected (higher resistivity without multi-step ionization), but the breakdown times were not particularly affected. Small amounts of air impurity were also added in an attempt to match the experiments. Although specific cases could be matched by varying these values, in general, quantitative agreement could not be achieved over a wide range of parameters.

The inherent assumption of a uniform electric field in the global model is likely a poor representation of the evolution of the discharge. There are at least three classes of discrepancies. The first class is the propagation delay for the avalanche front in traversing from the anode to the cathode, which, for the conditions of interest, can be a significant fraction of the breakdown time. The second class is non-uniformities in the electric field resulting from the shape and placement of electrodes and ground planes. These geometrically produced non-uniformities have another level of complexity resulting from charging of the capacitance of the dielectric walls of the discharge tube, which affects both the direction and magnitude of the local electric field [9]. The third class is enhancement and deformation of the electric field resulting from charge density in the avalanche front [36–38]. Since ionization coefficients are usually exponential functions of E/N , transport coefficients obtained using spatial averages of E/N are accurate only under select conditions. These conditions occur at higher values of E/N , where propagation delays are smaller fractions of the breakdown time and the enhancement in E/N in the avalanche front is smaller, at least on a relative basis. To quantitatively match experiments these spatial dynamics should be addressed.

5. Spatial dynamics of breakdown in Ar/Xe mixtures

In this section, results from 2-d modelling of plasma properties using LAMPSIM and their comparison with experiments will be discussed. The base case is Ar, 30 Torr and $V_0 = 2000$ V. Preionization electrons are generated on a continuous basis by photoionization from the external lamp as described in part I, producing an initial uniform density of 10^6 cm^{-3} (fractional ionization 10^{-12}). The unstructured mesh representing the lamp geometry contains 5561 nodes with spacings of 0.0075 cm near the electrodes to 0.0125 cm in the bulk plasma. The temperatures of the electrodes and discharge tube walls were held constant at 300 K during the simulation as the energy deposition during a single avalanche breakdown is insufficient to produce a significant temperature rise. One run of the 2-d model required 10–24 h (depending on the gas mixture and voltage waveform) on one processor of a Compaq Alphaserver ES-40 (833 MHz).

The electron density leading to breakdown for the base case is shown in figure 4. The electric potential, E/N and electron impact ionization source, S_e , are shown in

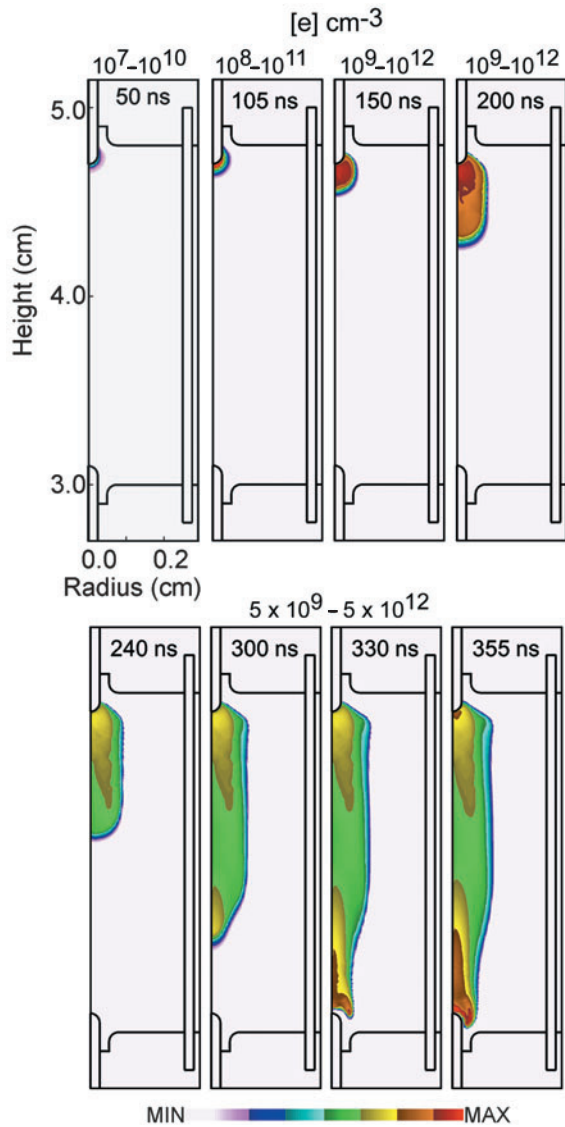


Figure 4. Electron density at different times during breakdown for the base case conditions (Ar 30 Torr, $V_0 = 2000$ V). The range of electron density (log scale, cm^{-3}) is shown at the top of each frame. Avalanche begins at the anode and propagates with a speed of $\approx 6 \times 10^6 \text{ cm s}^{-1}$.

figures 5–7, respectively. As the voltage ramps up, electric field enhancement at the anode produces ionization sources, which generate an electron density of 10^9 cm^{-3} close to the powered anode by 75 ns. Electron impact ionization and secondary emission from the cathode produce an electron density of only $\approx 10^7 \text{ cm}^{-3}$ near the cathode. This discrepancy is in large part due to the smaller degree of electric field enhancement at the cathode for this geometry. The drift of electrons towards the anode and ions toward the cathode in the high E/N near the tip of the anode results in charge separation. This separation produces a large E/N that initiates an avalanche front that is directed from the powered anode towards the grounded cathode beginning at ≈ 100 ns [36–38]. The avalanche reaches the cathode at ≈ 350 ns, producing a propagation delay of 250 ns or an avalanche speed of $6.4 \times 10^6 \text{ cm s}^{-1}$. Upon arrival of the avalanche front, the peak electron density is $\approx 1.5 \times 10^{13} \text{ cm}^{-3}$ close to the cathode.

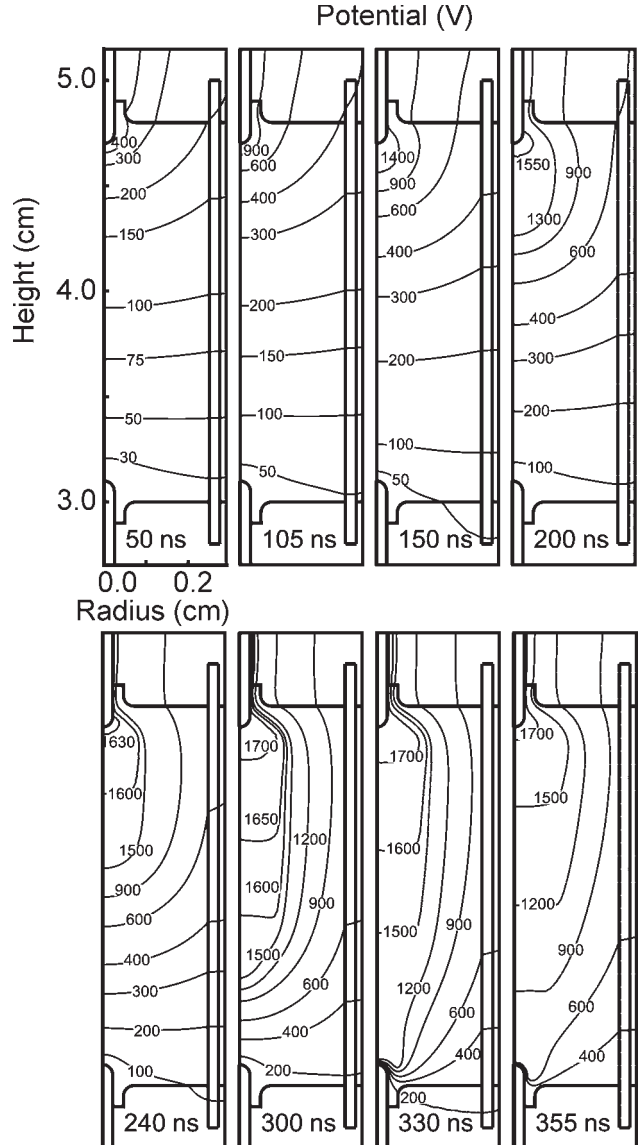


Figure 5. Electric potential at different times during breakdown for the base case conditions (Ar 30 Torr, $V_0 = 2000$ V). Higher conductivity in the ionized regions behind the avalanche front compresses potential ahead of the ionization front.

The ionized region trailing behind the avalanche front has $[e] \approx 10^{11} - 10^{12} \text{ cm}^{-3}$, with larger values near the electrodes and smaller values in the middle of the tube.

E/N and T_e along the axis are shown in figure 8. (Note that some of the noise in these plots results from interpolation from the unstructured mesh.) Initially, E/N is high near the powered electrode largely due to geometrical enhancement. When the avalanche is initiated, the peak E/N near the powered electrode (105 ns) is $\approx 850 \text{ Td}$ ($1 \text{ Td} = 10^{-17} \text{ V cm}^2$). As the ionization front propagates across the gap, the plasma is ionized, producing a conductive channel. E/N drops in the conductive plasma behind the avalanche front to 15–30 Td, thereby reducing the rate of ionization and lowering the voltage drop behind the front. Compression of the remaining voltage at the leading edge and in front of the avalanche adds to the enhancement of the local electric field. As the avalanche front moves into the bulk plasma, the peak E/N weakens to

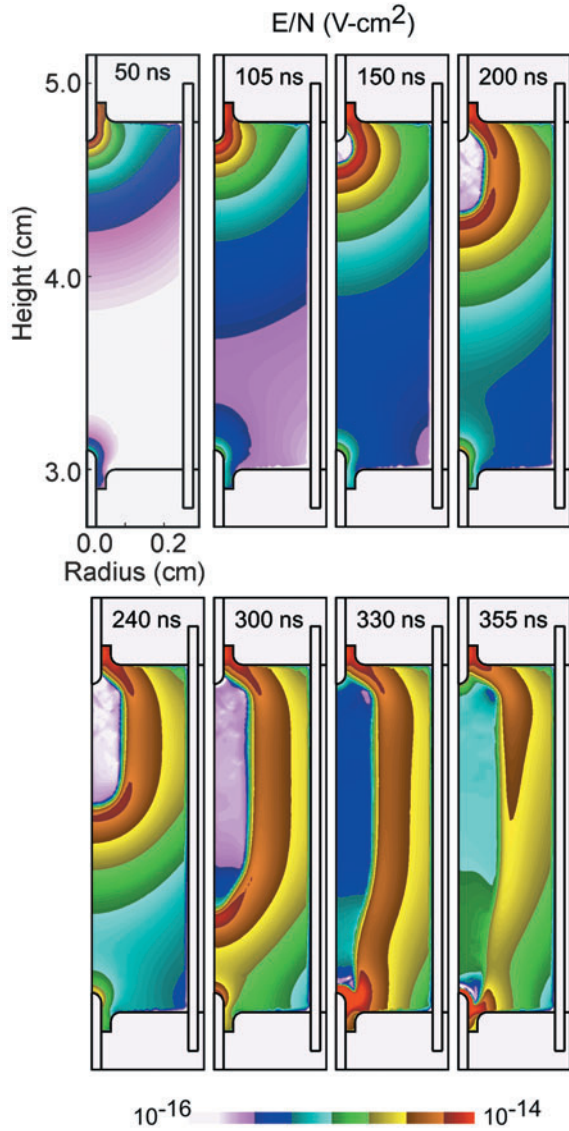


Figure 6. The magnitude of E/N (log scale, $V\text{ cm}^{-2}$) is shown at different times during breakdown for the base case conditions (Ar 30 Torr, $V_0 = 2000\text{ V}$). E/N peaks in the ionization front and increases in magnitude approaching the cathode due to voltage compression and geometrical enhancement.

500–600 Td in the absence of the geometrical enhancement at the anode. This large value of E/N is sustained almost totally by space charge. As the avalanche front approaches the cathode, E/N increases due to increasing amounts of voltage compression, increasing space charge and geometrical enhancement at the cathode. The E/N near the cathode is 1000–3000 Td at breakdown (355 ns). This high value of E/N is in large part due to voltage compression and space charge as the enhancement in E/N due solely to geometry is 100–200 Td. The radial width of the ionized region behind the avalanche front is essentially constant at the centre of the tube but narrows approaching the cathode. The narrowing of the ionized region follows the convergence of the electric field lines in the vicinity of the cathode.

T_e along the axis of the discharge tube is shown in figure 8(b). Peak values of $T_e = 6\text{--}7\text{ eV}$ occur at the edge of the ionization front where the electric fields are high. These values

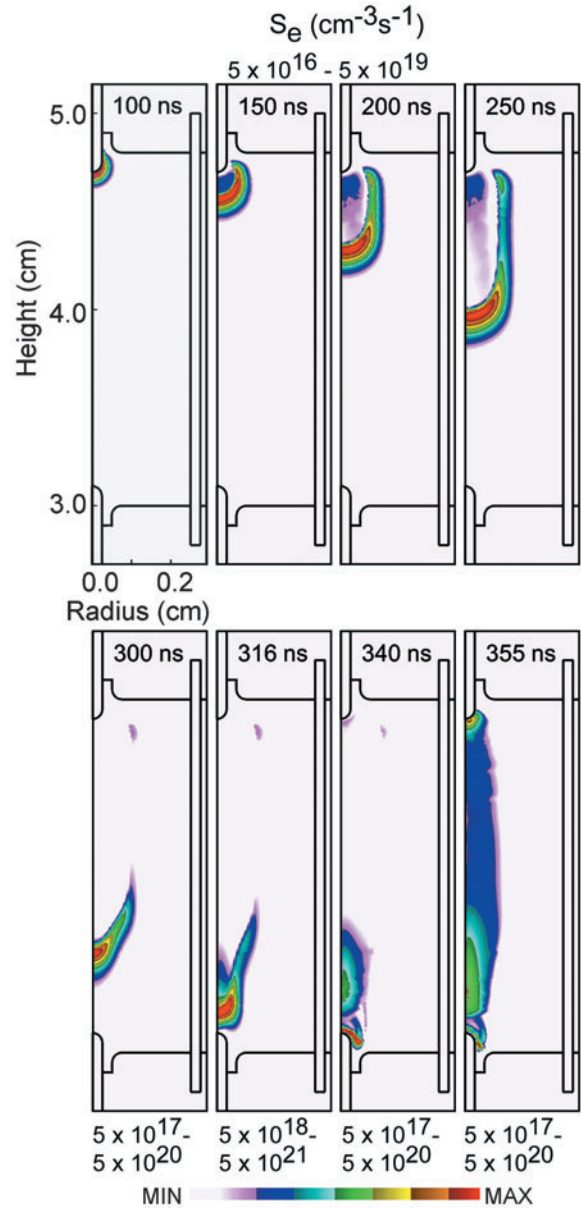


Figure 7. Electron impact ionization sources at different times for the base case conditions (Ar 30 Torr, $V_0 = 2000\text{ V}$). The ranges of values plotted ($\text{cm}^{-3}\text{ s}^{-1}$, log scale) are shown by each frame. The peak in sources occurs coincident to the peak in E/N as the high electric field crosses the inter-electrode gap.

of T_e generally exceed those obtained with the global model because the peak electric fields at the head of the avalanche front exceed the spatially averaged values used in the global model. In the conductive region behind the front, T_e falls to 3.5–4.0 eV, which is sufficient to sustain the plasma density but not increase its density. The large T_e at the leading edge of the front produces the large electron impact ionization sources shown in figure 7. The peak values of S_e are $5 \times 10^{19}\text{ cm}^{-3}\text{ s}^{-1}$ in the leading edge of the ionization front and fall to $10^{16}\text{--}10^{17}\text{ cm}^{-3}\text{ s}^{-1}$ in the ionized regions behind the front. As more voltage is compressed into the weakly preionized region ahead of the avalanche, T_e increases ahead of the front. This voltage compression also contributes towards increasing the peak T_e at the head of the avalanche front, another effect not accounted

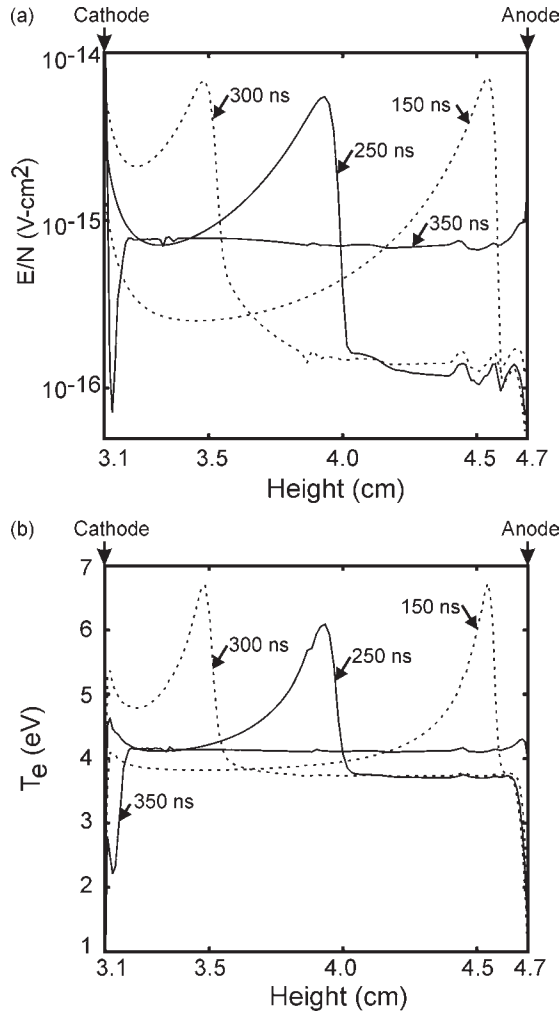


Figure 8. Plasma properties along the axis of the discharge tube at different times for the base case conditions (Ar 30 Torr, $V_0 = 2000$ V). (a) E/N and (b) T_e . The peaks indicate the location of the ionization front that propagates from the anode to the cathode. (Propagation is right to left.)

for in the global model. Small source terms appear ahead of the avalanche due to seeding by photoionization, which is then multiplied by the increasing T_e ahead of the avalanche.

As the avalanche front approaches the cathode (316 ns), S_e increases to as large as $10^{21} \text{ cm}^{-3} \text{ s}^{-1}$, which is supported by a T_e of 8.5–9.0 eV. When the plasma bridges the gap and the conductivity is more uniform across the gap, the electric field also becomes more uniformly distributed between the cathode and the anode. As a result, E/N increases in the bulk plasma to 60–80 Td, which raises electron impact sources to 10^{18} – $10^{19} \text{ cm}^{-3} \text{ s}^{-1}$ and T_e to ≈ 4 eV, while decreasing S_e and T_e near the cathode. The increase in E/N in the bulk plasma sustains the avalanche, increases the conductivity of the plasma and increases the current, which produces the voltage drop signifying breakdown. An anode-directed avalanche begins in this higher E/N region but quickly weakens as the total voltage drop across the gap decreases.

The mean time for conversion of Ar^+ to Ar_2^+ is $\approx 1 \mu\text{s}$ at 30 Torr, and so Ar^+ is largely the dominant ion in the plasma on the timescales of the breakdown. The density of Ar^+ just ahead of the avalanche front is 10^7 – 10^8 cm^{-3} and is

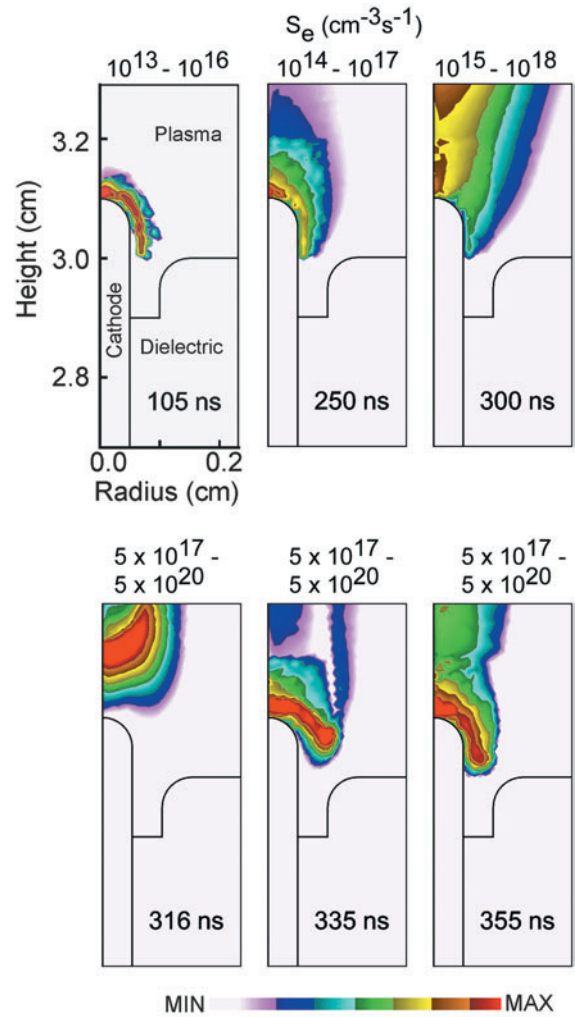


Figure 9. Electron impact ionization sources due to secondary electrons in the vicinity of the cathode at different times during breakdown for the base case conditions (Ar 30 Torr, $V_0 = 2000$ V). The ranges of values plotted ($\text{cm}^{-3} \text{ s}^{-1}$, log scales) are indicated by each frame. Ionization by secondary electrons rapidly increases as the ionization front approaches the cathode. Voltage compression and increased rates of photo-emission produce more ionization.

$\approx 10^{11} \text{ cm}^{-3}$ in the avalanche front. When the avalanche closes the gap, the ion density near the cathode peaks at $5 \times 10^{12} \text{ cm}^{-3}$ and is 10^{11} – 10^{12} cm^{-3} along the axis of the arc tube. The ion density adjacent to the walls is 10^7 – 10^8 cm^{-3} , whereas $n_e \approx 10^6 \text{ cm}^{-3}$. As these densities at the wall are near or below the ambipolar limit, the more mobile electrons in the periphery of the lamp freely diffuse to the walls, negatively charging the walls. A positive space charge region develops close to the walls. The wall charging process is rapid, and by 100 ns the walls are nearly fully negatively charged. The ionization front itself has a positive space charge.

Secondary emission of electrons from the cathode results from photoemission and ion bombardment. At the voltages and electrode temperatures of interest, electric field-enhanced thermionic emission is not important, as the work function of tungsten is 4.3 V, though unresolved surface roughness on the cathode with its accompanying electric field enhancement could produce minor electric field emission under select

conditions [39]. The photoemission of electrons into the large E/N near the cathode produces energetic secondary electrons and significant sources of ionization in spite of the large gas pressure.

The ionization sources due to electrons emitted from the cathode are shown in figure 9 for the base case. Prior to arrival of the avalanche front at ≈ 300 ns, the ion density near the cathode is small and so secondary emission is dominated by photoemission resulting from externally and plasma generated photons. The E/N at the cathode at this time is small (≈ 120 Td), and so the ionization by secondary electrons is small. As the ionization front approaches the cathode, voltage compression increases E/N at the cathode, while the rate of secondary electron emission increases due to photons generated by the nearing plasma. The end result is a significant increase in ionization by secondary electrons near the cathode at 250–300 ns. Peak ionization sources due to secondary electrons rise to $10^{19} \text{ cm}^{-3} \text{ s}^{-1}$ at 355 ns when the avalanche front arrives. It is at this time that ion bombardment replaces photoelectric emission as the principal source of secondary electrons and the E/N at the cathode peaks due to voltage compression. As the E/N decreases near the cathode with the onset of breakdown, ionization by secondary electrons also decreases in spite of there being a larger current of secondary electrons due to ion bombardment. It is expected that ion bombardment will continue to be the principal means of secondary emission in the glow phase as the discharge becomes self-sustaining.

Photoionization and photoemission play an important role in propagating the ionization front to produce gap closure. For these conditions, in the absence of photoionization there is insufficient voltage to fully close the gap. We computationally found that in the absence of photoionization the propagating avalanche front stalls near the centre of the discharge where the geometric electric field enhancement is at a minimum. The difficulty of obtaining breakdown for these conditions is qualitatively confirmed by experiments where breakdown is at best inconsistent in the absence of a UV source, as discussed in part I.

Predictions of mean breakdown times obtained with LAMPSIM as a function of Xe addition to Ar are shown in figure 10 and are compared with the experiments discussed in part I. In all cases, τ initially decreases with the addition of Xe, with minimum breakdown times occurring for 5–15% Xe across a wide range of pressures and voltages. Breakdown times increase with Xe addition above 15–20% and increase above that for pure Ar for xenon fractions of $>50\%$. The agreement with experiment of predicted breakdown times from LAMPSIM is systematically better for than for results obtained with GLOBAL_KIN due to the former's ability to resolve the dynamics of the avalanche front.

Note that breakdown is not obtained for all combinations of pressures, compositions and applied voltages, as discussed in part I. For example, breakdown does not occur at 90 Torr for Xe fractions of above 0.8 with $V_0 = 2000$ V. For these conditions the avalanche cannot be maintained, as the decrease in electron temperature in the avalanche front produced by momentum transfer and inelastic losses is not adequately compensated for by the lower ionization potential of Xe.

In a 30 Torr, Ar/Xe = 90/10 mixture, breakdown occurs at 275 ns. The electron density and ionization sources at this

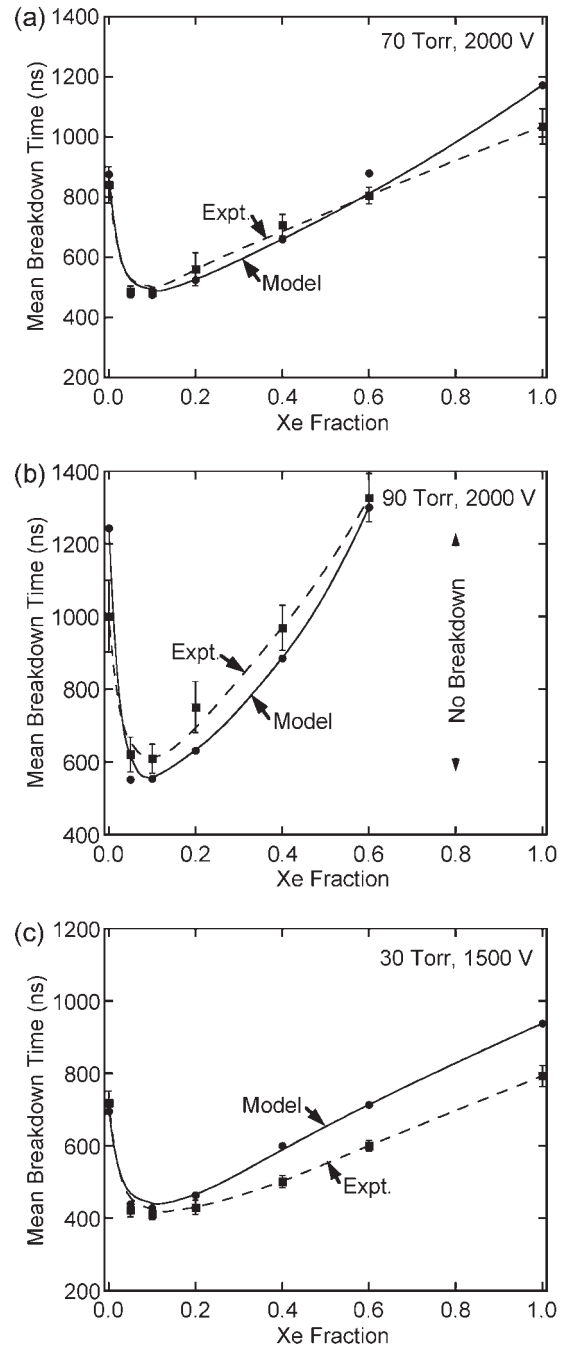


Figure 10. Breakdown times as a function of Xe fraction in Ar/Xe mixtures from the 2-d model and experiments. (a) 70 Torr, $V_0 = 2000$ V; (b) 90 Torr, $V_0 = 2000$ V and (c) 30 Torr, $V_0 = 1500$ V. Small additions of Xe (5–15%) minimize the breakdown time.

time are compared with those obtained in pure Ar in figure 11. E/N and T_e along the axis are shown in figures 12 and 13. While the avalanche has bridged the inter-electrode gap in the Ar/Xe mixture, the avalanche front has covered just half this distance in Ar. These trends result from two causes. First, the critical $(E/N)_0$ for the Ar/Xe = 90/10 mixture is smaller than for pure Ar, and so the avalanche is initiated earlier. Second, the speed of the avalanche is higher in the Ar/Xe mixture, as shown in figure 12. In pure Ar, the avalanche progresses

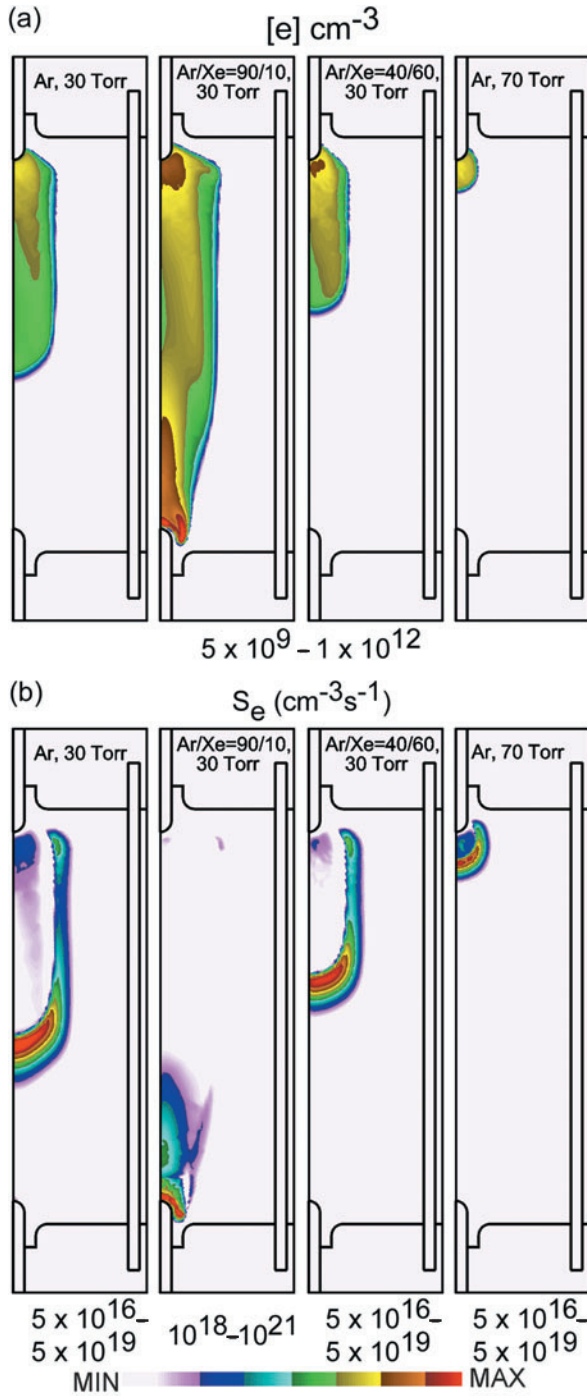


Figure 11. Plasma properties at 275 ns with $V_0 = 2000$ V for different gas mixtures and pressures: (a) electron density and (b) electron impact ionization sources. The ranges of values plotted (log scale) are indicated by each frame. The disparity in breakdown times is shown by the position of the avalanche front during its propagation from the anode to the cathode.

at $\approx 6.3 \times 10^6$ cm s $^{-1}$, whereas in Ar/Xe = 90/10 the speed is $\approx 1.2 \times 10^7$ cm s $^{-1}$. The higher speed of the ionization front results from the net rate of electron generation being higher due to the lower threshold processes in the mixture. The peak electron temperatures are lower in the Ar/Xe mixtures, which vary between 5–6 eV at the ionization front, compared with

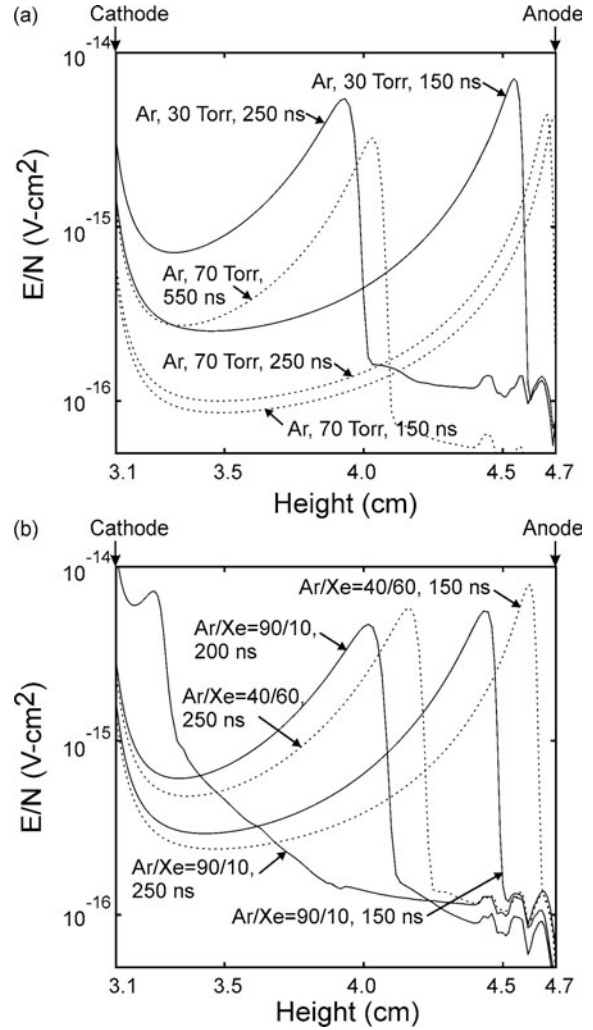


Figure 12. The magnitude of E/N (log scale, V cm 2) along the axis of the discharge tube for (a) Ar, $V_0 = 2000$ V, at 30 and 70 Torr and (b) 30 Torr, $V_0 = 2000$ V at 10 and 60% Xe fractions. (Propagation is right to left.) The speed of the ionization front is highest in the Ar/Xe = 90/10 mixture.

6–7 eV in pure Ar. In spite of both E/N and T_e being lower in the Ar/Xe mixture, the lower ionization thresholds in Xe compensate and the rate of net ionization is higher.

The fraction of Ar $^+$ of the total ion density is shown in figure 14(a) for the Ar/Xe = 90/10 mixture. In the ionization front, where the peak E/N is 400–500 Td and T_e is 5–6 eV, Ar $^+$ is the dominant ion. This dominance in large part results from two causes. First, Ar simply has the larger mole fraction. Second, the electron temperature is sufficiently high that the ionization rate coefficient for Ar is significant in spite of its higher ionization potential. The dominant ion in the ionized channel behind the front is Xe $^+$, which is 60–80% of the total ion density. The large fraction of Xe $^+$ in the channel results from the lower T_e , which now clearly favours the lower ionization potential of Xe. The lifetime of Ar $^+$ for charge exchange to Xe is ≈ 26 μ s, and so charge exchange is not a major loss process for Ar $^+$ on these timescales. The density of Ar(4p) is comparable with Ar $^+$ (10^{11} cm $^{-3}$) in the ionized regions, as shown in figure 15. The Ar(4p) density behind the avalanche front remains high (10^{10} – 10^{11} cm 3) throughout

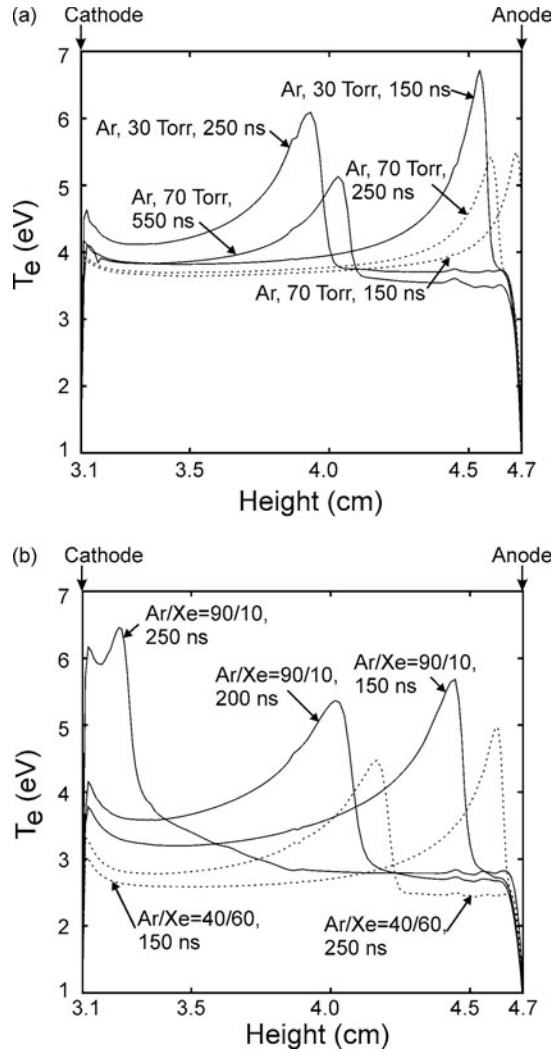


Figure 13. The electron temperature along the axis of the discharge tube for (a) Ar, $V_0 = 2000$ V at 30 Torr and 70 Torr and (b) 30 Torr, $V_0 = 2000$ V with 10% and 60% Xe fractions. (Propagation is right to left.) The peak electron temperature is lower at a higher pressure and larger Xe fraction.

the breakdown process, producing a rate of Penning ionization of Xe of $\gtrsim 10^{18} \text{ cm}^3 \text{ s}^{-1}$. This process is a major source of electron generation and could in part account for the large fraction of Xe^+ .

The plasma dynamics occurring in an Ar/Xe = 40/60 mixture are quantitatively different from those occurring in an Ar/Xe = 90/10 mixture. For example, E/N and T_e along the axis are shown in figures 12(b) and 13(b) for these mixtures. The peak E/N in the ionization front for the Ar/Xe = 40/60 mixture, 700–800 Td, is higher, while the speed of the ionization front is lower at $4.3 \times 10^6 \text{ cm s}^{-1}$. The lower electron temperature of 4.5–5.0 eV at the ionization front in ArXe = 40/60 results from higher rates of momentum transfer and inelastic losses, which shift the EED towards lower energies. This ultimately reduces the ionization rates and increases the breakdown time. Xe^+ is the dominant ion in the ionization front, as shown in figure 14, since Xe constitutes the major fraction of the mixture, its ionization potential is lower and T_e is lower than in the more dilute mixtures.

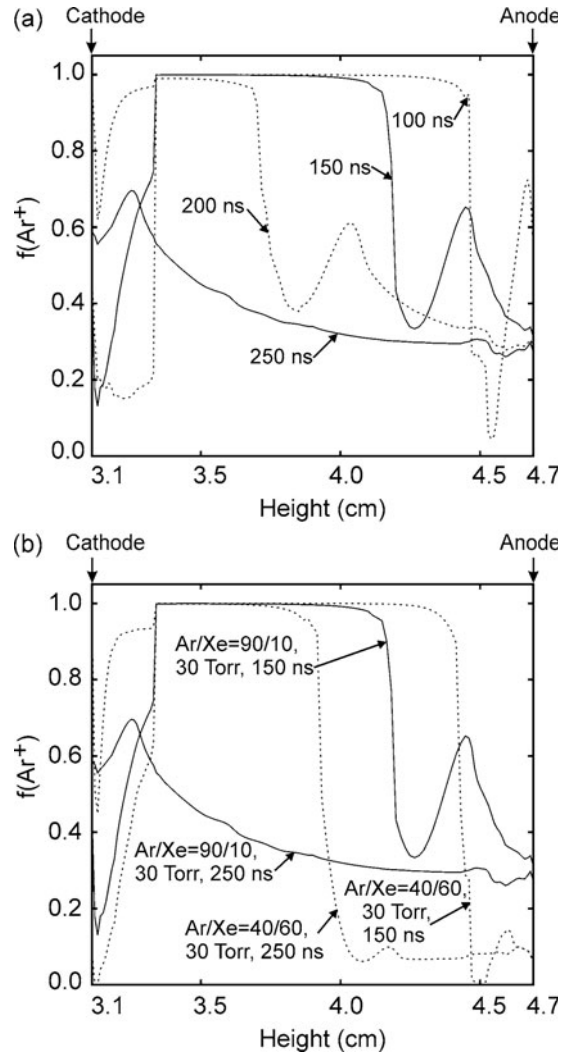


Figure 14. The fraction of Ar^+ ions along the axis of the discharge tube for (a) Ar/Xe = 90/10, 30 Torr, $V_0 = 2000$ V and (b) 30 Torr, $V_0 = 2000$ V for 10% and 60% Xe. (Propagation is right to left.) The Ar^+ fraction decreases behind the ionization front.

The fraction of Ar^+ in the ionized regions behind the front at 250 ns decreases from 30–35% for Ar/Xe = 90/10 to 8–10% for Ar/Xe = 40/60. The $\text{Ar}(4p)$ density is also lower ($\approx 10^{10} \text{ cm}^{-3}$) and its peak moves with the ionization front (figure 15). With the lower T_e , production of excited states of Xe is favoured over $\text{Ar}(4p)$, and the quenching of $\text{Ar}(4p)$ by collisions with Xe is more rapid. Therefore, unlike the Ar/Xe = 90/10 case, the rates of Penning ionization of Xe by $\text{Ar}(4p)$ are large and important in the ionization front ($10^{18} \text{ cm}^3 \text{ s}^{-1}$) but are negligible in the ionized regions behind the front.

The effects of pressure on the breakdown dynamics are less dramatic. The electron density and ionization sources are shown for Ar at 70 Torr in figure 11 at 275 ns. E/N at the ionization front in the base case is 600–650 Td and is 300–420 Td at 70 Torr. This is in part simply due to the increase in pressure and partly due to less charge separation owing to the lower mobilities of charge carriers. The peak T_e (4.5–5.5 eV) and peak electron impact source terms ($2 \times 10^{19} \text{ cm}^{-3} \text{ s}^{-1}$) in the ionization front are both lower at 70 Torr compared with

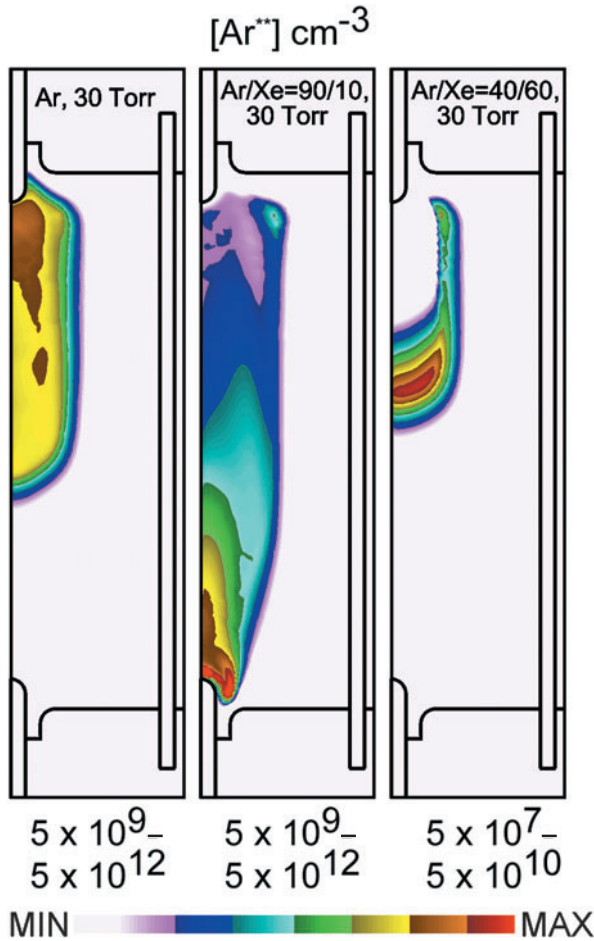


Figure 15. The density of Ar^{**} (log scale, cm^{-3}) at 230 ns for $V_0 = 2000$ V for different operating conditions. $[\text{Ar}^{**}]$ decreases at higher Xe content due to there being lower electron temperatures which result in lower production of Ar^{**} and increased rates of quenching.

the base case (see figures 11 and 13). The decrease in E/N and T_e in the ionization front leads to a decrease in the ionization rate coefficients and sources, and hence breakdown is slower at higher pressures. Computed breakdown times as a function of pressure are compared with experiments in figure 16 for $\text{Ar}/\text{Xe} = 95/5$ ($V_0 = 2000$ V), $\text{Ar}/\text{Xe} = 60/40$ ($V_0 = 2000$ V) and $\text{Ar}/\text{Xe} = 90/10$ ($V_0 = 1800$ V). In general, the agreement is good, showing an increased breakdown time with increasing pressure. For the larger V_0 , τ increases less rapidly at low pressures. This trend likely results from ionization rates saturating at large E/N . As the applied E/N decreases at higher pressures, the ionization rates decrease more rapidly and so τ increases.

The spatial dynamics of breakdown are sensitive functions of applied voltage. For example, E/N and ionization sources at 300 ns for 30 Torr of Ar for $V_0 = 1500$ and 2000 V are compared in figure 17. The peak E/N at the ionization front is 600 Td at 1500 V compared with 850 Td at 2000 V and weakens to ≈ 500 Td as the front progresses. The lower applied bias increases the delay before the critical E/N required for electron avalanche is reached. Once the avalanche begins, the speed of the ionization front is higher with the larger bias (6.3×10^6 cm s^{-1} at 2000 V compared with 3.7×10^6 cm s^{-1} at

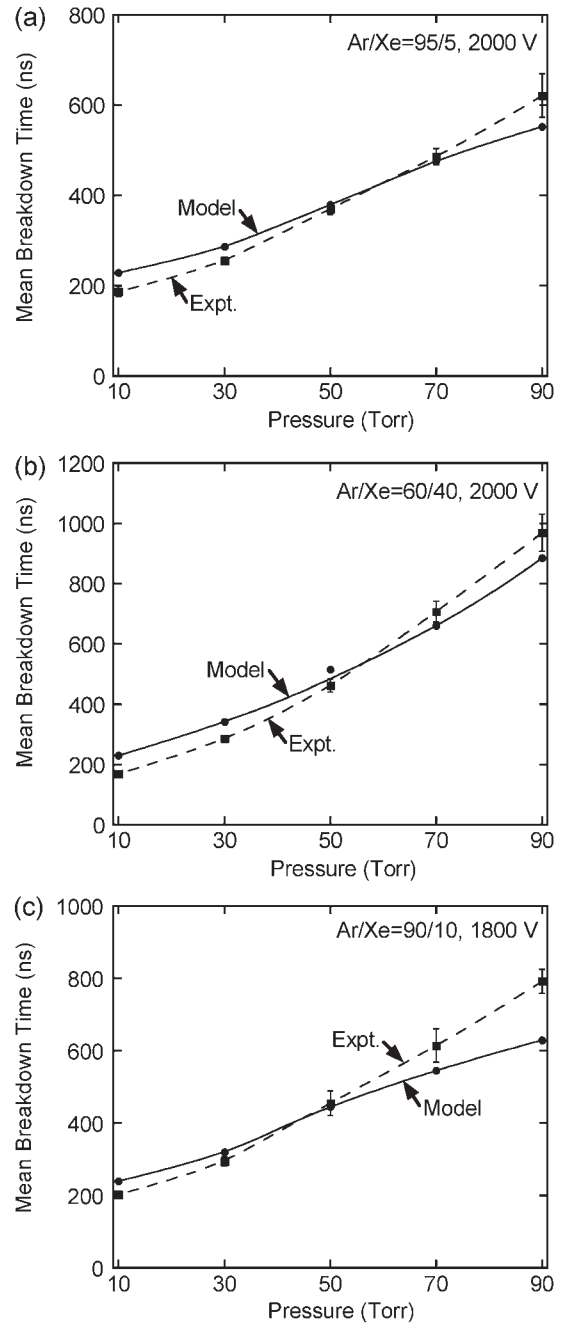


Figure 16. Breakdown times obtained from the 2-d model and experiments as a function of pressure for (a) $\text{Ar}/\text{Xe} = 95/5$, $V_0 = 2000$ V; (b) $\text{Ar}/\text{Xe} = 60/40$, $V_0 = 2000$ V and (c) $\text{Ar}/\text{Xe} = 90/10$, $V_0 = 1800$ V.

1500 V). E/N in the gas ahead of the ionization front is lower at 1500 V (10–30 Td) than at 2000 V (50–100 Td), leading to electron impact sources that are two orders of magnitude lower than at 2000 V. Both these factors decrease the rate of electron avalanche towards the cathode at 1500 V.

The mean breakdown time as a function of applied voltage is shown in figure 18 for $\text{Ar}/\text{Xe} = 90/10$ at 10 and 30 Torr and Ar at 30 Torr. As V_0 increases from 800 to 1000 V for $\text{Ar}/\text{Xe} = 90/10$ at 10 Torr, the breakdown time falls sharply from 800 to 500 ns. The decrease, however, is asymptotic,

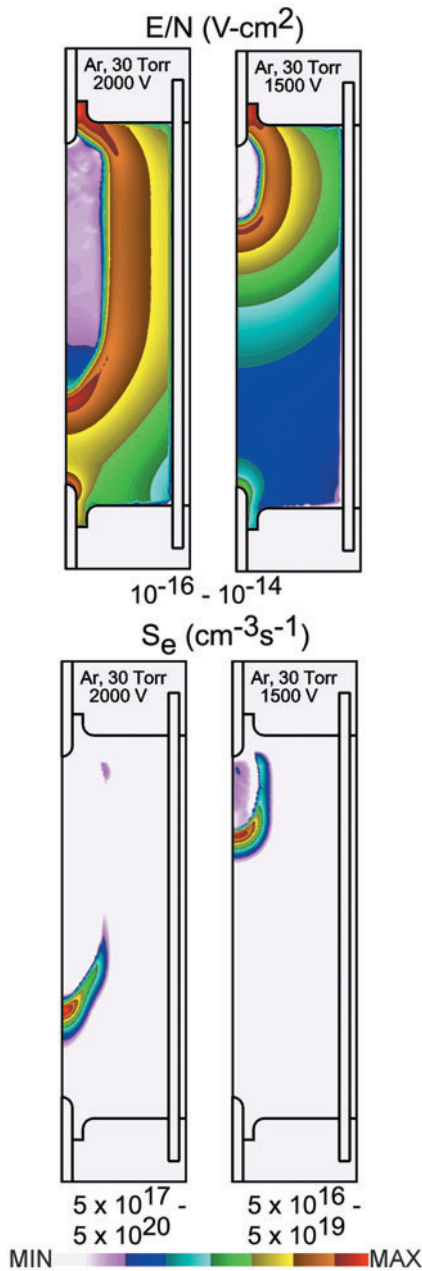


Figure 17. Plasma properties for Ar at 300 ns for $V_0 = 2000$ V and 30 Torr: (a) E/N and (b) electron impact ionization sources. The ranges of values plotted (log scale) are indicated by each frame.

and beyond $V_0 = 1400$ the breakdown times do not change significantly. Similar trends are obtained at higher pressures and in pure Ar. The cause for this saturation in τ with increasing voltage is likely the behaviour of the ionization rate coefficient with E/N . The ionization rate coefficient of Ar saturates at $\approx 10^{-8} \text{ cm}^3 \text{ s}^{-1}$ for values of E/N above 1000 Td, as shown in figure 19. Although this higher range of E/N is not accessed based on the applied V_0 , these values are approached or exceeded in the ionization fronts, with the peak E/N in the ionization fronts increasing with increasing V_0 . As such, once the E/N in the avalanche front approaches 1000 Td, further increases in V_0 will probably not result in significant increases in ionization sources. As a result,

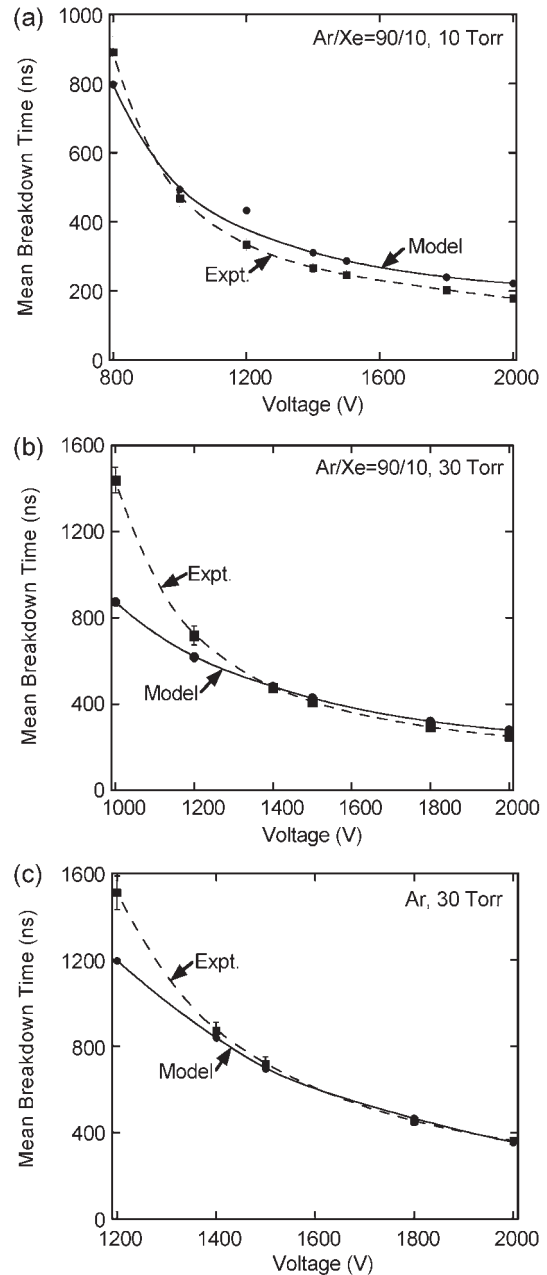


Figure 18. Breakdown times obtained from the 2-d model and experiments as a function of applied voltage for (a) Ar/Xe = 90/10, 10 Torr; (b) Ar/Xe = 90/10, 30 Torr and (c) Ar at 30 Torr.

the speed of the ionization front approaches an asymptotic value. The agreement between results from the model and experiments is systematically better at higher values of V_0 . These trends are likely a result of the lower V_0 cases being more sensitive to secondary processes such as photoionization and UV photoemission from the electrodes, which are at best approximated in the model.

The breakdown times predicted by the global model were not particularly sensitive to the excited states kinetics as the ionization was dominated by electron impact from ground states during an avalanche. Breakdown times from the 2-d model were, however, quite sensitive to excited state kinetics. This sensitivity was in large part due to changes

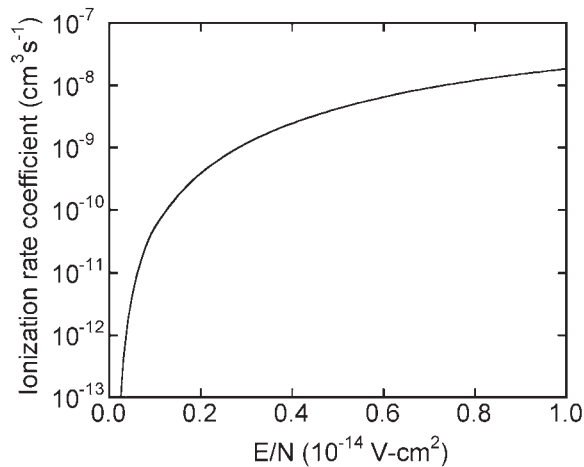


Figure 19. The ionization rate coefficient of Ar as a function of E/N . Rate coefficients increase by two orders of magnitude as E/N increases from 100 to 500 Td. Beyond 1000 Td, the rate coefficient saturates.

in conductivity of and voltage drop across the ionized region behind the avalanche front, which in turn changed the amount of voltage dropped across the avalanche front and the low conductivity region in advance of the front. For example, excluding excited stated ionization and Penning processes increased the voltage drop across the conduction channel, thereby reducing the voltage drop across the low conductivity region and lengthening the breakdown time. Quantitative agreement with experiment using the 2-d model required a nearly full set of kinetics.

6. Concluding remarks

Results from global and 2-d modelling studies of breakdown process in Ar/Xe mixtures using a model lamp geometry were discussed. Modelling predictions of breakdown times were compared with experimental data reported in part I. Results from the global model reasonably agree with the experimental trends; however, breakdown times are under-predicted over a large range of compositions, pressures and voltages. This disagreement is likely a result of propagation delays of the avalanche front and non-uniformities in plasma parameters such as the electric field, which are not captured in the global model.

The 2-d model is able to capture the spatial and temporal dynamics during breakdown. Results from the 2-d model show a Townsend-like propagation of the ionization front from the anode to the cathode with a finite propagation time leading to breakdown. Ionization following secondary electron emission from the cathode contributes to closure of the inter-electrode gap. The secondary emission is largely dominated by photoemission in the early stages of breakdown and provides an increasingly important source of ionization as voltage compression increases E/N at the cathode as the gap is closed.

The computed breakdown times from the 2-d model agree well with experimental data. Lower applied voltages increase breakdown times by delaying the critical E/N needed to

avalanche the gas. The ionization rates are decreased at higher pressures due to lower electron temperatures in the avalanche front resulting from the lower applied E/N . Small fractions of Xe (5–15%) in Ar decrease the breakdown times by providing a low threshold energy component for electron impact ionization and by providing a Penning ionization partner. Larger Xe fractions increase momentum transfer and inelastic losses that decrease the electron temperature at the ionization front, leading to lower ionization rates and longer breakdown times.

Acknowledgments

This work was supported by the General Electric Research and Development Center, by the National Science Foundation (CTS 03-15353) and by the Computational Science and Engineering Program at the University of Illinois at Urbana-Champaign. The authors thank Drs Timothy Sommerer and David Wharmby for their advice during this investigation.

References

- [1] Byszewski W W and Budinger A B 1990 *J. Illum. Eng. Soc.* **19** 70
- [2] Byszewski W W, Li Y M, Budinger A B and Gregor P D 1996 *Plasma Sources Sci. Technol.* **5** 720
- [3] Zaslavsky G, Cohen S and Keffe W 1990 *J. Illum. Eng. Soc.* **19** 76
- [4] Gregor P D, Li Y M, Budinger A B and Byszewski W W 1996 *J. Illum. Eng. Soc.* **25** 150
- [5] Pitchford L C, Peres I, Liland K B, Boeuf J P and Gielen H 1997 *J. Appl. Phys.* **82** 112
- [6] Pejovic M M, Ristic G S and Karamarkovic J P 2002 *J. Phys. D: Appl. Phys.* **35** R91
- [7] Smith D and Zhu H 1993 *J. Illum. Eng. Soc.* **22** 27
- [8] Gibson R G 1994 *J. Illum. Eng. Soc.* **23** 19
- [9] Lay B M, Moss R S, Rauf S and Kushner M J 2003 *Plasma Sources Sci. Technol.* **12** 8
- [10] Moss R S, Eden J G and Kushner M J 2004 Avalanche processes in an idealized lamp. I: Measurements of formative breakdown time *J. Phys. D: Appl. Phys.* **37** 2502
- [11] Carleton S, Sienen P A and Stoffels J 1997 *J. Illum. Eng. Soc.* **26** 139
- [12] Hayashi M 1991 *Nagoya Institute of Technology Report No IPPJ-AM-19*
- [13] Tachibana K 1986 *Phys. Rev. A* **34** 1007
- [14] Rapp D and Englander-Golden P 1965 *J. Chem. Phys.* **43** 1464
- [15] McFarland R H and Kinney J D 1965 *Phys. Rev. A* **137** 1058
- [16] Vriens L 1964 *Phys. Lett.* **8** 260
- [17] Kannari F, Suda A, Obara M and Fujioka T 1983 *IEEE J. Quant. Electron.* **QE-19** 1587
- [18] Zapesochyni I P and Shimon L L 1966 *Opt. Spectrosc.* **11** 155
- [19] Biondi M A 1976 *Principles of Laser Plasmas* (New York: Wiley)
- [20] Mason N J and Newell W R 1987 *J. Phys. B: At. Mol. Opt. Phys.* **20** 1357
- [21] Hayashi M 1983 *J. Phys. D: Appl. Phys.* **26** 581
- [22] Eckstrom D J, Nakano H H, Lorents D C, Rothem T, Betts J A, Lainhart M E, Dakin D A and Maenchen J E 1988 *J. Appl. Phys.* **64** 1679
- [23] Johnson T H, Cartland H E, Genoni T C and Hunter A M 1989 *J. Appl. Phys.* **66** 5707
- [24] Suzuki T Y, Sakai Y, Min B S, Takayanagi T, Wakiya K and Suzuki H 1991 *Phys. Rev. A* **43** 5867
- [25] Ellis H W, Pai R Y, McDaniel E W, Mason E A and Viehland L A 1976 *At. Data Nucl. Data Tables* **17** 177
- [26] Holstein T 1951 *Phys. Rev.* **83** 1159
- [27] Shul R J, Passarella R, Upshulte B L, Keese R G and Castleman A W 1987 *J. Chem. Phys.* **86** 4446

- [28] Dorai R and Kushner M J 2002 *J. Phys. D: Appl. Phys.* **35** 2594
- [29] Rockwood S D 1973 *Phys. Rev. A* **8** 2348
- [30] Brown P N, Hindmarsh A and Byrne G D 1998
*VODE—Variable Coefficient Ordinary Differential
Equation Solver*
- [31] Kushner M J 2004 *J. Appl. Phys.* **95** 846
- [32] Skyblue Systems Inc., PO Box 14223, Albany, NY
12212-4223, <http://www.skybluesystems.com>
- [33] Scharfetter D L and Gummel H K 1969 *IEEE Trans. Electron.
Dev.* **ED-16** 64
- [34] SLAP Sparse Matrix Library, <http://www.netlib.org>
- [35] Seager M K 1998 *Lawrence Livermore National Laboratory
Technical Report UCRL-100195*
- [36] Kulikovskiy A A 2000 *J. Phys. D: Appl. Phys.* **33** 1514
- [37] Georghiou G E, Morrow R and Metaxas A C 2001 *J. Phys. D:
Appl. Phys.* **34** 200
- [38] Pancheshnyi S V and Starikovskii A Yu 2003 *J. Phys. D :
Appl. Phys.* **36** 2683
- [39] Sommerer T J, Pak H and Kushner M J 1992 *J. Appl. Phys.* **72**
3374